Magnetic ground states in nanocuboids of cubic magnetocrystalline anisotropy

Francisco Javier Bonilla, Lise-Marie Lacroix, Thomas Blon

Magnetic ground states in nanocuboids of cubic magnetocrystalline anisotropy

F.J. Bonilla[†], L-M. Lacroix, T. Blon[*]

INSA, UPS, LPCNO, CNRS-UMR 5215, 135 avenue de Rangueil, 31077, Toulouse, France

Abstract

Flower and easy-axis vortex states are well-known magnetic configurations that can be stabilized in small particles. However, <111> vortex (V<111>), *i.e.* a vortex state with its core axis along the hard-axis direction, has been recently evidenced as a stable configuration in Fe nanocubes of intermediate sizes in the flower/vortex transition. In this context, we present here extensive micromagnetic simulations to determine the different magnetic ground states in ferromagnetic nanocuboids exhibiting cubic magnetocrystalline anisotropy (MCA). Focusing our study in the single-domain / multidomain size range (10-50 nm), we showed that V<111> is only stable in nanocuboids exhibiting peculiar features, such as a specific size, shape and magnetic environment, contrarily to the classical flower and easy-axis vortex states. Thus, to track experimentally these V<111> states, one should focused on i) nanocuboids exhibiting a nearly perfect cubic shape (size distorsion < 12%) made of *ii)* a material which combines a zero or positive cubic MCA and a high saturation magnetization, such as Fe or FeCo; and *iii)* a low magnetic field environment, V<111> being only observed in virgin or remanent states.

Keywords: magnetic nanocubes, hard-axis vortex, flower-vortex transition, single-domain limit.

1. Introduction

Magnetic nanoparticles attract considerable scientific and technological interests in diverse applications such as biomedicine, magnetic recording, radio-frequency devices, etc. From a technological point of view, manufacturing of magnetic particles are carried out by various methods which allow the control of the shape, size, composition, crystallinity and thus of the magnetic properties. Among the different particles, rectangular cuboids constitute a large family that can be synthesized by chemical means to act as nanobiological vectors for drug delivery or as heat mediators for magnetic field

hyperthermia [1], using Fe [2], iron oxides [3-4], Co ferrite [5], Co oxide [6], FeCo [7], FePt [8] or Ni [9] materials. The understanding and engineering of individual nanomagnets is mandatory to optimize their properties in regards to the targeted applications. Whereas the single-domain magnetic configuration is typically required for applications such as permanent magnets and magnetic recording, more complex magnetic nanostructures such as vortices, domain walls and skyrmions are expected to play key roles in future memory devices. In a different context, vortex states are sought in biological applications to minimize the stray field around the magnetic particle and thus prevent aggregation. The exact description of the magnetic configuration of each nanomagnets within a more complex magnetic system is consequently a key factor driving the final physical properties.

From the modeling point of view, classical micromagnetics refers to uniform magnetization distributions that can only occur in ellipsoidal magnetic nanoelements [10]. Micromagnetic simulations have become essential to investigate spin arrangements in non-ellipsoidal nanomagnets, among which nanocuboids. In the last decades, lots of numerical efforts have been devoted on perfect nanocubes (NCs) with uniaxial anisotropy to determine the critical size separating single-domain and vortex configurations, referred to as the single-domain limit. Schabes and Bertram [11] initially showed that NCs below 50 nm exhibit a quasi-uniform distribution of moments along the [001] uniaxial easy-axis, known as flower state (hereafter named F[001]), while larger ones exhibit a vortex configuration, whose core axis lays along the [001] direction (hereafter named V[001]). Then, the single-domain limit in a cube has been proposed by the NIST's micromagnetic modeling group in the framework of the standard problem [12]. Different studies have addressed the single-domain limit in NCs with various uniaxial anisotropy [13-16], leading to stable twisted F<001> and V<001>, as well as metastable F<111> and V<111> states.

However, considering cubic anisotropy becomes essential since most of the chemically grown nanocuboids are prepared from materials exhibiting either positive or negative cubic magnetocrystalline anisotropy (MCA). While a positive cubic MCA results in <001> easy-axis, as in Fe, a negative anisotropy imposes <111> preferential directions, as in Ni and Fe_3O_4. Only few numerical studies have

been reported on NCs made of cubic MCA materials. Whereas a F<111> state was determined as the equilibrium state in Fe_3O_4 NCs over a large size range [17], a transition between F<111> and V<001> states was predicted in Ni NCs [18].

Experimental studies on the single-domain limit are now available thanks to the recent improvement of imaging techniques. Electron holography (EH) performed in a dedicated transmission electron microscope (TEM) allows mapping the magnetic induction with lateral resolution of 1-2 nm [19,20]. Moreover, EH recently became sensitive enough to investigate the flower/vortex transition in individual nanomagnets. A F<111> state has been measured in an isolated single crystal Fe_3O_4 nanocuboid of 50 nm [21], in good agreement with previous numerical studies [17]. A vortex state has been recorded as a function of temperature in a ~200 nm Fe_3O_4 particle [22]. Recently, we have reported a systematic study of the flower/vortex transition in isolated Fe NCs: F<001>, V<111> and V<001> states were evidenced at room temperature in 25, 26 and 27 nm NCs respectively [19]. Whereas F<001> and V<001> were expected for small and large NCs, respectively, the V<111>, *i.e.* a vortex state with a vortex axis along the Fe hard-axis direction, was unexpected. Indeed, while V<111> has been previously predicted numerically in Fe nanospheres, for diameters varying between 25 and 40 nm [23], it was only predicted as a metastable state in NCs of uniaxial [11] or cubic MCA [18]. Our recent observations evidenced that V<111> is a stable intermediate state within the flower/vortex transition of Fe NCs. Thus, numerous questions arisen about the effective stability of the V<111> spin arrangement in magnetic nanocuboids.

We report here numerical simulations on nanocuboids with cubic MCA to address the different magnetic ground states at room temperature in a size range between the exchange length $l_{ex} = (A/\mu_0 M_S^2)^{1/2}$ and the domain wall width $\delta_w = \pi(A/K_1)^{1/2}$. Our study aims at tracking the V<111> domain of stability at the frontiers between single-domain and multidomain states. The study is first focused on the magnetic nanoparticles measured experimentally [19], *i.e.* single-crystalline isolated Fe NCs (Section 3). As real nanomagnets usually exhibit a cuboid-like shape rather than a perfect cubic shape, the effect of an axial deviation from the perfect cubic shape is then studied and its influence on the V<111> stability

discussed (Section 4). The field dependence of the magnetic states in such cuboids is then addressed, the majority of EH experiments being performed at remanence or under a small *in-situ* magnetic field due to the pole piece stray field of the objective lens (Section 5). Finally, the variety of magnetic configurations that could be observed in ferromagnetic nanocubes of cubic MCA is studied for both positive and negative MCA NCs (Section 6). Different ferromagnetic materials are simulated such as Fe, FeCo (positive cubic MCA), Fe_3O_4, Ni (negative cubic MCA) and NiFe (nearly zero MCA). The magnetic parameters required to stabilize the V<111> state are finally summarized.

2. Ground state calculations in individual nanocuboids

In a ferromagnet, the magnetic state with the lowest energy results from the minimization of the total magnetic energy E_m, defined as the sum of $E_m = E_{ex} + E_{mc} + E_d + E_z$ (1), where E_{ex} is the exchange energy, E_{mc} is the magnetocrystalline energy, E_d is the dipolar energy and E_z is the Zeeman energy. In order to compute the NC energy minima, we performed micromagnetic calculations using OOMMF-3D package [24] following either *(i)* the dynamical or *(ii)* the conjugate-gradient (CG) approaches. The dynamical approach solves the Landau-Lifshitz-Gilbert (LLG) equation of motion and gives a rigorous solution. However, long simulation times are encountered to calculate dipole-dipole interactions. The second CG approach allows reaching a stable magnetic configuration after short computational times using the fast Fourier transform. In this case, the energy is minimized directly without taking into account the magnetization dynamics. Combining both CG- and LLG-algorithms allows to reduce the computing time [25] : CG-algorithm was first used to obtain a stable magnetic state which was then insert like a seed state for the LLG calculation.

Simulations were done by considering nanocuboids of edges *a*,*b*,*c* along *x*,*y*,*z* respectively. Results presented in sections 3, 4 and 5 were obtained for NCs with <001> crystalline directions along the cube edges (as experimentally encountered in ref. [19]) and magnetic parameters of bulk body-centered-cubic

(*bcc*) Fe at room temperature: saturation magnetization M_S = 1.71 MA/m, exchange stiffness A = 21 pJ/m and cubic anisotropy constant K_1 = 48 kJ/m^3 [26]. A damping parameter α = 0.5 was used to reach the equilibrium remanent state fairly rapidly. For the meshing, a cubic cell of (0.5×0.5×0.5) nm^3 was used, the lateral dimension being smaller than the exchange length in Fe ($l_{ex}=(A/\mu_0 M_S^2)^{1/2}$ = 2.4 nm).

In order to identify the ground state among the different metastable solutions that could be obtained, calculations were performed from various initial configurations of the magnetization. A first approach consisted in introducing a random orientation of the magnetic moments as the initial state. CG-simulations were stopped at convergence ($|\vec{m}\times\vec{H}\times\vec{m}|$ < 0.02 A/m) and the obtained configurations introduced as seed states in LLG-algorithms. The energy values were then tracked until the relaxation occurred ($d\vec{m}/dt$ < 0.002 deg/ns). Depending on the NC size, three different configurations could be reached by this means: flower, <111> and <001> vortices. A second approach consisted in imposing artificially the initial spin configurations following an homogeneous, V<111> or V<001> configurations. After relaxation, the comparison between the energies of these three magnetic configurations for a similar nanocuboid size allows to define unambiguously the ground state.

Note that in the following we use chevrons <*uvw*> and square brackets [*uvw*] to describe magnetic configurations. <*uvw*> is used when the symmetry axis of the considered configuration owns to the family of directions *uvw* without any distinctions. For example V<100> would mean V[100], V[010], V[001] or the negative of any of those directions: they all have the same energy. [*uvw*] is used when the symmetry axis is defined into a specified direction which cannot be associated with the corresponding family.

3. Stable magnetic configurations in perfect Fe nanocubes

Figure 1 shows the magnetic phase diagram of perfect Fe NCs (*a=b=c)* whose size is varied from 10 to 50 nm. The energy densities $e_m=E_m/V$, $e_{ex} = E_{ex}/V$, $K_{mc} = E_{mc}/V$, $K_d = E_d/V$ and $e_z = E_z/V$ obtained for each ground states are plotted on Fig. 1(a). Three different regions can be delimited :

(i) for a < 23.5 nm (in blue on Fig. 1(a)), the magnetic moments are mostly aligned along a <001> direction, *i.e.* along one of the positive MCA easy-axis. The corresponding configuration in Fig. 1(c) revealed the so-called flower state (F<001>) characterized by slightly tilted moments at the vertex.

(ii) for larger sizes i.e. a > 27 nm (in yellow), the magnetic moments tend to curl in the so-called vortex state, the vortex axis around which the moments rotate is along the <001> easy-axis directions (Fig. 1(e)).

(iii) for intermediate sizes, *i.e.* 23.5 nm ≤ a ≤ 27 nm (in white), the vortex axis is along a <111> direction, which corresponds to the MCA hard-axis direction. The V<111> configuration is clearly identified as the ground state in this size range by comparing the respective energies of the flower, the V<001> and the V<111> states, calculated for each size. For example, considering a = 25 nm, calculations give $e_m^{V<111>}$ = 0.54 MJ/m^3 < $e_m^{F<001>}$ = 0.56 MJ/m^3 < $e_m^{V<001>}$ = 0.63 MJ/m^3. A representative V<111> state observed in a 25 nm NC is shown in Fig. 1(d); the rotation of the magnetic moments along the <111> diagonal is clearly seen.

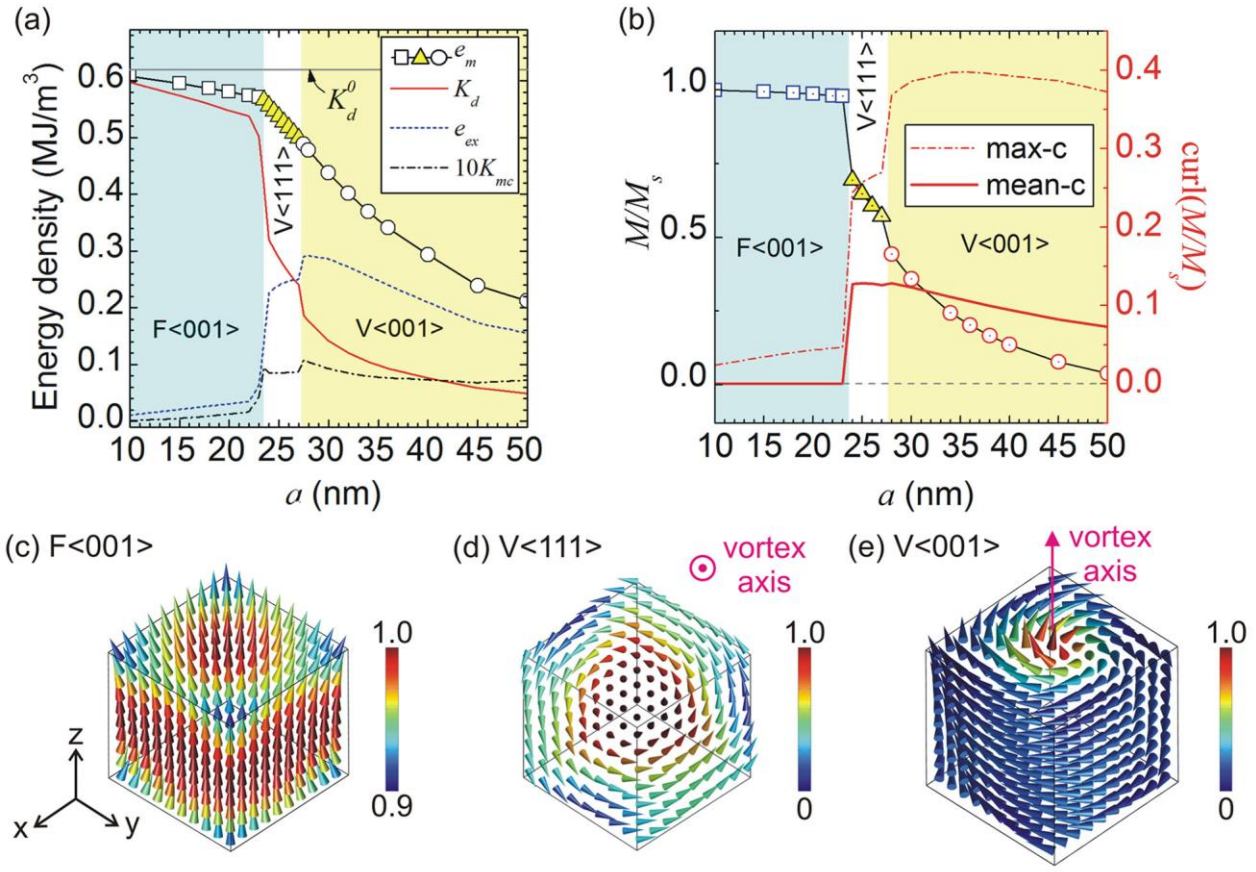

Figure 1. (a) Energy densities of magnetic ground states as a function of edge-cube size *a*. *Dots*: total magnetic energy density e_m (*square*, *triangle*, and *circle* dots correspond to F<001>, V<111> and V<001> respectively). *Solid-red line*: dipolar ($K_d = E_d/V$), *dashed-blue*: exchange ($e_{ex} = E_{ex}/V$) and *black dash-dots*: magnetocrystalline ($K_{mc} = E_{mc}/V$) energy densities. (b) Normalized magnetization as a function of size (black dots), and calculated max-curling and mean-curling quantities of the magnetization vector field as a function of NC size. Simulated 3D-magnetic configurations: (c) F<001> (20 nm NC), (d) V<111> (25 nm, projected along [111]) and (e) V<001> (30 nm).

In order to characterize these three different states, the magnetization *curling* field $\left(\vec{\nabla} \times \frac{\vec{m}}{M_s}\right)$ was computed on the whole NC volume. Such curling field allows a global description of any rotating fields, such as the magnetization in a vortex state. Two scalar parameters are extracted:

(i) the mean curling, which stands the averaged circulation of the magnetization $\vec{m}$ in the NC, $\left|\left\langle \vec{\nabla} \times \frac{\vec{m}}{M_s} \right\rangle\right| = \frac{1}{n}\left\|\sum_{i=1}^{n} \vec{\nabla} \times \left(\frac{\vec{m_i}}{M_s}\right)\right\|$ (3)

where *i* represents each cell in the discretized volume of *n* cells.

(ii) the max-curling, which is the maximum value of the curling field :

$$\left(\left|\vec{\nabla} \times \frac{\overrightarrow{m}}{M_s}\right|\right)_{MAX} = max\left(\left\|\vec{\nabla} \times \left(\frac{\overrightarrow{m_i}}{M_s}\right)\right\|\right) \quad (4)$$

The max-curling allows discussing local rotations without facing averaging effects encountered with the mean-curling. For instance, quasi-uniform vector fields, such as the magnetization in a flower state configuration, will present a mean curling ~ 0, but a max-curling which can deviate from 0 due to rotation at vertex.

3.1 Flower state (*a* < 23,5 nm)

If one considers a perfect single-domain, consisting in an homogenous arrangement of moments oriented along one of the MCA easy axis, e_{ex} and K_{mc} are expected to be constant and fairly low. The main energy contribution arises from the K_d term due to the presence of magnetic charges at the surfaces, edges and corners of the NCs [27,28]. A dipolar energy density $K_d^0 = {}^1/_6\,\mu_0 M_s^2$ independent of the cube size can be estimated. Even if such a perfect state cannot be rigorously obtained in a cube due to the non-uniform demagnetizing field induced, K_d approaches $K_d{}^0$ for NCs with $a < l_{ex}$ (Fig. 1(a)). Above this size, the moments tend to partially rotate, as evidenced by a non-zero max-curl parameter (Fig. 1(b)). The curling field reaches a maximum value at the cube's vertex, but is globally compensated over the whole volume, keeping therefore the mean-curl parameter negligible. Flowering thus allows efficiently lowering the dipolar term, but at the expense of the exchange term. Fig. 1(a) evidences the progressive enhancement of the flowering through the increase of the max-curl and e_{ex} terms and the decrease of the K_d up to the flower/vortex transition observed for a cube size of ~10 l_{ex}.

3.2 <111> and <001> vortex states ($a \geq 23.5$ nm)

The vortex type configurations lead to a drastic reduction of the dipolar energy K_d but to an increase of the exchange and magnetocrystalline terms. Fig. 2(a)-(b) display the 3D magnetization in V<111> and V<001> states. An iso-*M* surface is plotted, evidencing the spins for which $M'/M_S = 0.8$, where *M'* is the component of the magnetization along the vortex axis, *i.e.* $M'=M_{111}$ and $M'=M_{001}$ for V<111> and V<001>, respectively. The iso-M surface encloses a large region in V<111>, leading to a global magnetization amplitude M/M_S above 0.6 (Fig. 1(b)). On the contrary, the reduced core region in V<001> allows reducing M/M_S below 0.5. The mean-curling curve in Fig. 1(b) exhibits a maximum for the V<111> configuration. Such an effect can be understood since the spins in the large V<111> tend to rotate from their <111> direction in the core to become parallel to the surfaces on facets, to reach a stray-field-free configuration.

To further describe the different vortex structures, the magnetic configuration in a median plane perpendicular to the vortex axis is represented in V<111> (25 nm NC) and three V<001> (30, 34 and 42 nm NCs) configurations in Fig. 2(c). As the exchange energy imposes a minimal misalignment between neighboring spins, the progressive spin rotation from an out-of-plane direction in the core to a pure in-plane direction at peripheries cannot be fully achieved neither in V<111> nor in small V<001> (30 nm NC). For a 34 nm NC (V<001>), in-plane magnetization is only reached at the extreme corners, while in-plane magnetization is fully stabilized on the whole lateral facet for a 42 nm NC. By further increasing the cube size, the moments at the NC's corners tend to be aligned antiparallel to the vortex axis, leading to a reduced remanent magnetization (Fig. 1(b)): above 65 nm, M/M_S tends to zero due to the presence of "down" corners surrounding the "up" core, initiating the multidomain configuration observed at larger sizes.

As a conclusion, V<111> is only stable in a limited size range (23.5 - 27 nm) as intermediate between F<001> and <001> vortex. The fairly similar exchange and dipolar energy densities, combined with the higher M/M_S value and the lateral extend of the iso-*M* surface, indicates that V<111> is a more

homogeneous configuration than V<001>. These results on Fe NCs are in good agreement with the EH measurements which reports a V<111> in a 23.5 nm Fe NC surrounded with a 1 nm Fe_3O_4 shell [19]. The thin oxide shell did not play any significant role as revealed by previous simulations.

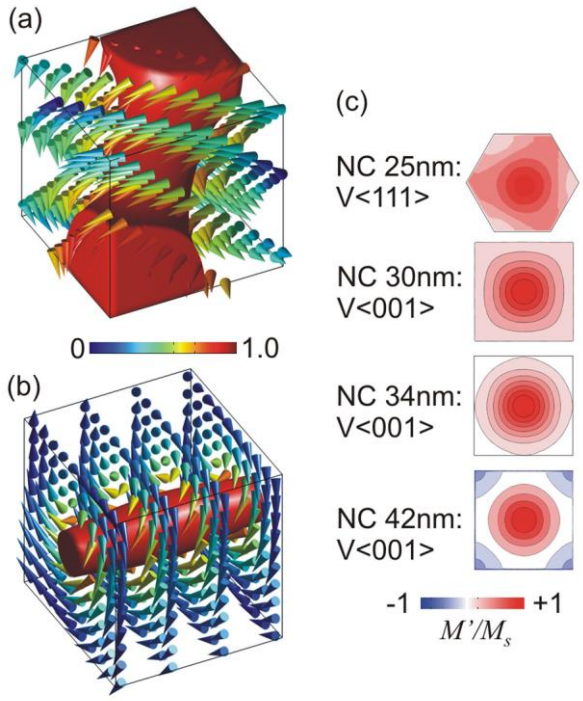

Figure 2. Simulated 3D-magnetic configurations of (a) V<111> (25 nm) and (b) V<001> (30 nm). The red iso-*M* surface enfolds the magnetic moments whose component along the vortex-axis is M'/M_S = 0.8 ($M'=M_{111}$ and $M'=M_{001}$ for V<111> and V<001> resp.). (c) Simulated magnetizations in the median plane (perpendicular to the vortex-axis) for different NC sizes.

4. Deviation from the perfect cubic shape

The experimental syntheses of perfect cubic particles still remains challenging, rectangular cuboids, *i.e.* parallelepipeds with rectangular faces, being mostly obtained. The unique experimental evidence of V<111> states has been reported for Fe NCs presenting some shape deviation (c/a ~ 17%) [19]. While a perfect cube do not own any shape anisotropy, deviations from the perfect cubic shape automatically

induce preferential magnetization direction(s) imposed by dipolar considerations. Thus one can question the stability of V<111> in real cuboids and the maximum deviation accepted. It should be noted that truncated corners appear in real nanoparticles, as a result of surface energy minimization, but, in a first approach, we did not consider this effect.

A cube belongs to the parallelepiped group and has its edge-sizes $a=b=c$. We focused our study on square cuboids for which at least two faces are squares, that is $a = b \neq c$. By fixing $a=b$ we studied in details two types of Fe cuboids, the elongated ($c>a$) and the flattened ($c<a$) ones. This situation is particularly relevant to analyze EH results because, as a TEM technique, EH gives only a 2D projection of the sample. Therefore, the thickness c is unknown and has to be assumed from the lateral dimensions. Figure 3(a) shows the magnetic-state phase diagram for Fe cuboids, where the background lines indicate the cuboid effective size $t = (a \times a \times c)^{1/3}$ allowing to compare the cuboid volume with a cube of an effective volume t^3.

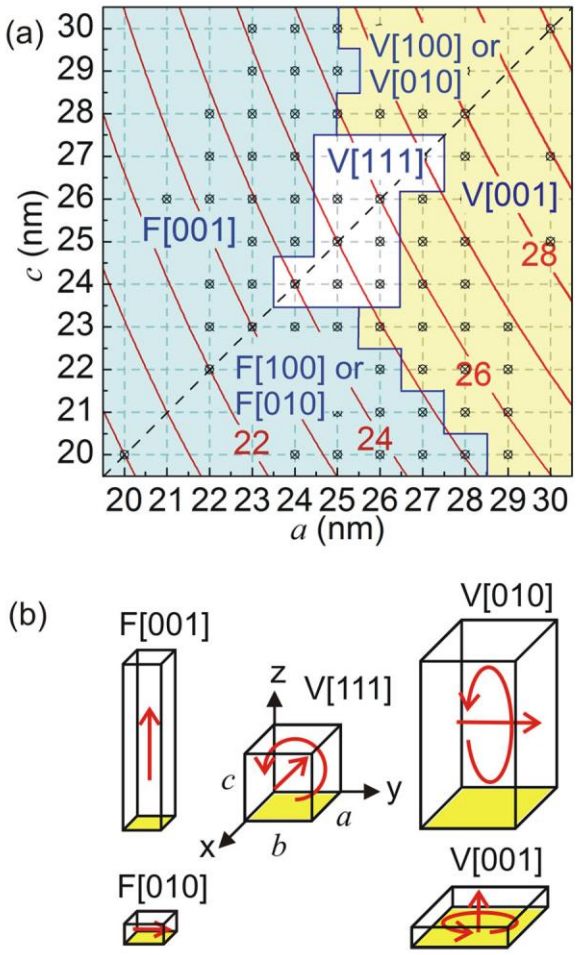

Figure 3. (a) Magnetic configurations as a function of a and c cuboid edge sizes. The background lines correspond to the particle effective size $t = (a \times a \times c)^{1/3}$ (diagonal dashed line: case of cubes, *i.e.* $a=b=c$, dots: sizes of simulated cuboids). (b) Sketches of configurations obtained in (a).

The main dashed diagonal in Figure 3(a) corresponds to the previous case of a perfect Fe NCs (section 3), with the three F<001>, V<111> and V<001> states being stable solutions. Considering now cuboids, the flower configuration appears to be the ground state for small ones, while <001> vortex is stabilized in larger objects ($a > 10\ l_{ex}^{Fe}$). In the intermediate size range, V<111> is only observed in cuboids with effective sizes t corresponding to 10 – 11 times l_{ex}^{Fe}, as in the case of perfect NCs. Moreover, V<111> is only stable for a limited aspect ratio range, $0.89 < c/a < 1.12$, that is, for size deviation ($|c-a|/a$) smaller than 12%. In other words, the existence of the V<111> intermediate state in cuboids is limited to rather cubic particles. It means that the two measured V<111> in ref. [19] were probably obtained in specific

Fe NCs presenting smaller cubic deviations than the averaged 17% deviation determined on the whole batch.

For larger deviations, V<111> is no longer stabilized, flower and easy-axis vortices were the only states observed. These states are no longer degenerated, cuboid asymmetry leading to an effective shape anisotropy. F[100] (or F[010]) are favored for small flattened cubes, while F[001] are observed in elongated ones (Fig. 3(b)). Removing degeneracy is also observed in cuboids presenting <001> vortices. For large flattened cuboids (under the dashed diagonal in Fig. 3(a)) V[001] is stabilized. Indeed, the spin curling benefits from the largest area of the (*xOy)* basal plane to reduce the misalignment between neighboring spins and consequently the exchange energy (V[001] in Fig. 3(b)). Similarly, large elongated cuboids (above the dashed diagonal) present a vortex axis perpendicular to the deviation axis (V[010] in Fig. 3(b)).

In summary, five different magnetic configurations could be distinguished in the phase diagram of cuboids. Considering $a = b \neq c$, F[100] and F[010] (V[100] and V[010]) are energetically equivalent but differs from F[001] (V[001] resp.). On the other hand, the four possible <111> vortices in a cuboid remain equivalents, due to the limited cubic deviation allowed.

5. Magnetic field dependence of the magnetic configurations

Previous sections were focused on virgin ground states obtained in absence of any external magnetic field, *i.e.* e_z = 0 in Eq. (1). While the magnetization reversal has been numerically studied in NCs of sizes corresponding to quasi-uniform and <001> vortex remanent states [11,18,29], the magnetization reversal of the V<111> state is particularly detailed here. Fig. 4 displays the magnetization reversal of 20, 25 and 30 nm Fe NCs of respective F<001>, V<111> and V<001> virgin states (Section 2). The hysteresis loops were calculated for magnetic field applied along the [001] easy-axis and ranging from $\mu_0 H_z$ = + 5 T to – 5 T with 1 mT steps. For the sake of readability, the loops displayed in Fig. 4 are only focused on the +700 mT to -700 mT field range.

As expected for F<001>, a square hysteresis loops is obtained (Fig. 4(a)). A sharp switching from F[001] to F[00-1] is observed, without the appearance of any other magnetic configurations. Considering small ellipsoid of positive cubic MCA, one expects a switching field of $2K_1/\mu_0 M_S$ = 56 mT for Fe [30,31]. Such a value is however only approached for reduced NC size, while switching field above 100 mT is encountered for a 20 nm NC: as previously reported numerically for uniaxial NCs [11], flowering in NCs of positive cubic MCA results in a so-called configurational anisotropy which increases the switching field.

For a 30 nm NC exhibiting a V<001> virgin state (Fig. 4(c)), a flower state F[001] is observed for high magnetic fields. A V[001] is then stabilized below a switching field (+150 mT in Fig. 4(c)), whose value increases with the NC size (not shown). The configuration change leads to a significative drop of the magnetization. At $\mu_0 H_z = 0$, the NC exhibits a V[001] remanent state as the virgin ground state (point 1 and corresponding snapshot in Fig. 4(c)). The magnetic configuration further evolved with the applied field leading to a linear decrease of *M(H)*. Indeed, moments surrounding the +*z* vortex core progressively turn into the –*z* direction. At the coercive field ($\mu_0 H_C$ = -150 mT, point 2 in Fig. 4(c)), the magnetic configuration corresponds to a +*z* compressed core surrounded with -*z* reversed moments leading to $M/M_S = 0$. As the applied field approaches saturation at point 3, the core is even more compressed. The final step of the reversal then corresponds to an abrupt reversal of the core resulting in a F[00-1] at saturation (~ -500 mT).

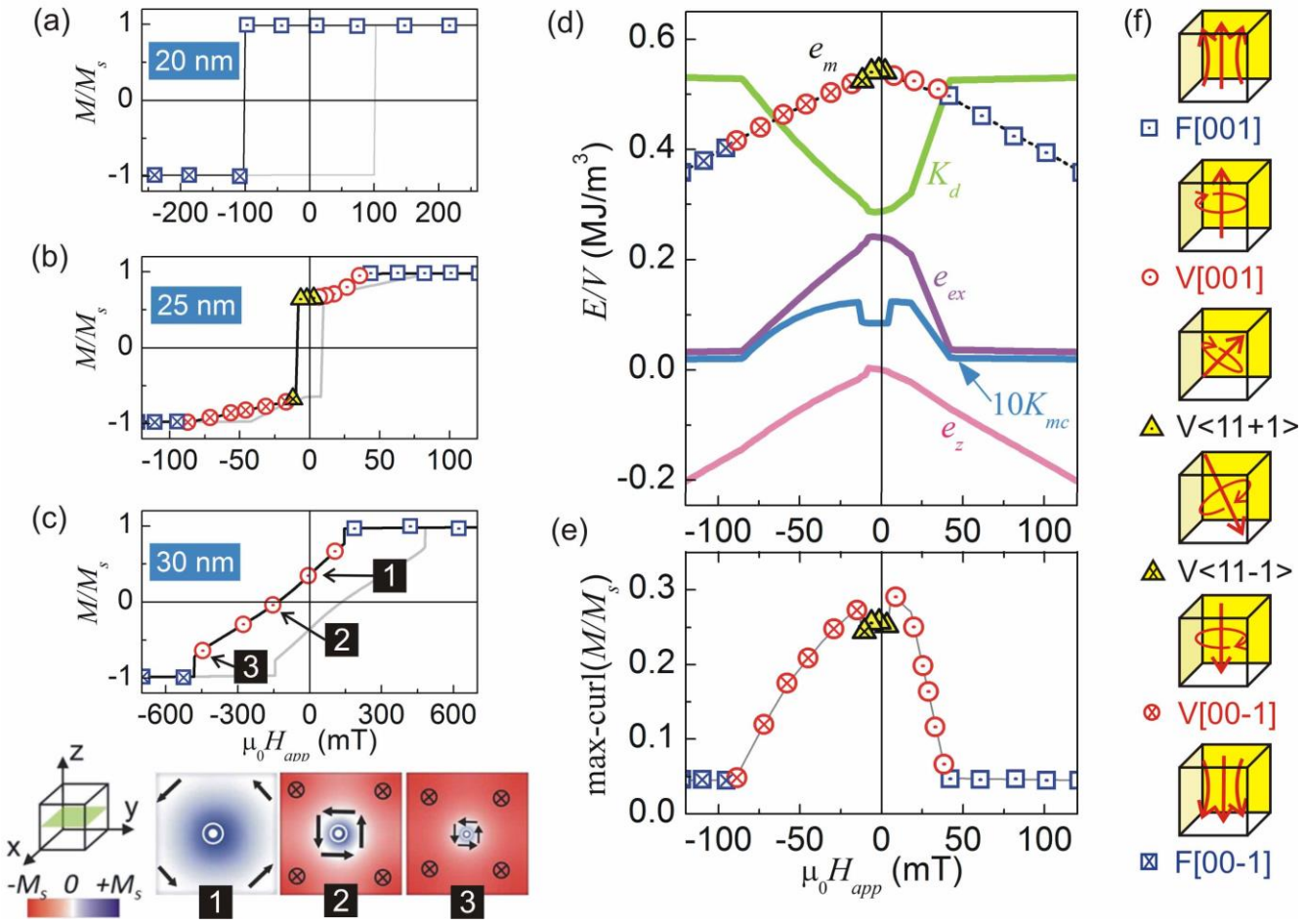

Figure 4. Magnetization reversal as a function the applied magnetic field (along [001]) in three representative Fe NCs of (a) 20 nm, (b) 25 nm and (c) 30 nm, corresponding to the three reported virgin ground states, F<001>, V<111> and V<001>, respectively. The dots in the hysteresis loops correspond to the different configurations displayed in (f). Three snapshots of the magnetization in the median plane corresponding to the points 1, 2 and 3 in (c) are inserted. Colorbar gives the M_z magnitude, the arrows sketch the magnetization directions. (d) Magnetic energies and (e) max-curling evolutions during the magnetization reversal of a 25 nm Fe NC. (f) Schematic views of the magnetic configurations encountered during the magnetization reversal of a 25 nm NC: the sequence of configurations observed in a field sweep from positive ([001]) to negative ([00-1]) is indicated from top to bottom.

Figure 4(b) displays the magnetization reversal in a 25 nm cube, which exhibits V<111> as virgin ground state, for an applied field along the [001] easy-axis direction. F[001] configuration is

encountered for $\mu_0 H_z$ > 40 mT. This quasi-uniform state has a high dipolar energy cost but minimizes the exchange and Zeeman terms (Fig. 4(d)). At +40 mT, the flowering opens around the *z*-direction, leading to a V[001] state. For 40 mT > $\mu_0 H_z$ > 10 mT, the max-curling in Fig. 4(e) increases as a result of variations of the [001] vortex structure. This modification of the vortex structure comes along with variations in dipolar, exchange and magnetocrystalline energy densities and results in a decrease of the magnetization. It could be noted that the V[001] state stabilized in this field range is not strictly identical to the V[001] reported in Fig. 1 where no field is applied. Indeed, max-curling values for V[001] at $H \neq 0$ (Fig. 4(d)) are smaller than for V[001] at $H=0$ (Fig. 1(b)), indicating that the curling is lower due to the Zeeman interaction. Therefore, the V[001] stabilized under magnetic field tends to be more homogenous than without applied field, leading to larger values of the K_d term compared to the virgin V[001] displayed in Fig. 1(a). Reaching the zero field value, V[001] becomes energetically unfavorable and a V<111> is stabilized. The magnetization reversal can be summarized as a rotation of the whole vortex structure with the vortex axis flipping from [001] into one of the <11+1> directions (one of the [11+1], [1-1+1], [-11+1], [-1-1+1] directions). As described in the schematics of Fig. 4(f), the reversal from +*z* towards –*z* direction is then carried out by rotating the V<11+1> axis to V<11-1> (one of the [11-1], [1-1-1], [-11-1], [-1-1-1] directions) at -10 mT. Moments in the <11-1> vortex core maintain a component along the field direction minimizing the Zeeman energy. For larger fields between -10 mT and -85 mT, the vortex axis rotates to the [00-1] direction and the max-curling progressively drops as a result of the homogenization of the magnetic structure. The transition to F[00-1] finally completes for $\mu_0 H$ = -85 mT. Simulations for different NCs in the V<111> size range ($23.5 \leq a \leq 27$ nm) have confirmed the representativity of such a 25 nm Fe NC.

To conclude, the magnetization reversal in a <111> NC contrasts with the one reported for <001> vortex. Whereas the magnetization reversal in NCs > 27 nm operates *via* reversed moments around the vortex core, NCs with $23.5 \leq a \leq 27$ nm reverse *via* the rotation of the whole vortex structure. A noticeable point is that, whatever the virgin configurations, the remanent states always correspond to the

virgin states previously found. It allows for instance to experimentally observe V<111> configurations in appropriate NCs at remanence, even after saturation in a <001> magnetic field.

6. Magnetic configurations in NCs made of various materials of cubic MCA

As the stable spin configuration is guided by the balance between exchange, dipolar and magnetocrystalline energies which scale with A, M_S^2 and K_1 intrinsic parameters respectively, it is strongly material dependent. Iron oxides, ferrite and iron based alloys (FeCo, permalloy) are examples other than iron of abundantly used nanoparticles displaying cubic MCA. Previous sections have shown that <111> vortices can be stabilized in nanocuboids of positive cubic MCA. Would V<111> be stable in NCs made of other materials and particularly in negative MCA materials ?

Table I compares the magnetic parameters for some magnetic materials with cubic MCA. FeCo alloy is the only material exhibiting a stronger saturation magnetization (M_S) than Fe. Fe and FeCo present the highest A and K_{mc} values, these parameters being reduced in others materials.

Material	M_S (MA/m)	A (pJ/m)	K_1 (kJ/m^3)
Fe	1.71	21	48
$Fe_{0.65}Co_{0.35}$	1.95	26	20
$Fe_{0.20}Ni_{0.80}$	0.83	10	-1
Ni	0.49	9	-5.2
Fe_3O_4	0.48	7	-13

Table I. Magnetic data of magnetic materials with cubic crystalline structures [26,32].

Figure 5(a) shows the magnetic phase diagram of NCs made of the different materials listed in Table 1. In $Fe_{0.65}Co_{0.35}$ NCs, the flower/vortex transition is similar to the one observed in Fe NCs, with successive

F<001>, V<111> and V<001> states. However the higher M_S decreases the transition size window due to the predominance of the dipolar contribution.

In FeNi alloy, the transition occurs at larger sizes and involves only F<001> and V<001> states. The lower moment of FeNi reduces the dipolar effect and favors flower state even for large sizes, as previously suggested in spheres [33].

At the opposite, Ni and Fe_3O_4 present a large reduction of the total energy density due to low values of M_S, A and K_1. The negative K_1 values in these materials result in F<111> magnetic configurations on the whole studied size range. F<001> is never observed, as previously reported for Ni [18]. Combined with a low saturation magnetization, the <111> easy-axis flower persists to large sizes, with a F<111>/V<001> transition at 58 nm for Fe_3O_4, without any V<111> intermediate state. Such results are in good agreement with the experimental imaging of a F<111> state in a 50 nm Fe_3O_4 faceted nanoparticle [21], even if it has been shown that significant faceting in nanocuboids can induce differences in the ground states with respect to perfect nanocube [34].

A deeper analysis can be performed considering finer variations of the magnetic parameters. Indeed, the tuning of the Fe-concentration in alloyed NCs can be seen as an effective tool to modulate the magnetic parameters. For instance, Slater-Pauling curve suggests a progressive M_S increase with Fe content in FeNi alloy. Moreover, due to size effect, nano-objects can exhibit magnetic parameters which deviates from the bulk values [35], thus assessments on the magnetic parameters dependence is mandatory. For this purpose, simulations of NCs were carried out with extreme values of M_S, A and K_1. The limits were chosen to contain the magnetic parameters presented in Table 1. Fig. 5(b) shows the phase diagrams for NCs having a combination of the following magnetic parameters: M_S = 1.95, and 1.0 MA/m; K_1 = 50, 0 and -30 kJ/m^3; and A = 7, 14 and 21 pJ/m.

Several tendencies can be extracted from the 9 graphs presented in Fig. 5(b). For a fixed M_S, the larger size at which flower state can still be observed, referred to as the critical size, increases with the exchange constant A. For instance, comparing frames 1, 2 and 3 for M_S =1.0 MA/m, this critical size

increases from 22 nm to larger than 30 nm with A. For M_S = 1.95 MA/m, this critical size evolves from less than 15 nm to 22 nm for A = 7 pJ/m and A = 21 pJ/m, respectively. This is clearly expected as exchange tends to favor uniform arrangements.

The reinforcement of quasi-uniform state with A is also found for K_1 <0. Nevertheless the M_S amplitude has in this case a major influence on the orientation of the flower state. For low and moderate M_S, as in Fe_3O_4 NCs and M_S = 1.0 MA/m in frames 7-8-9, the magnetic moments mainly align along the <111> direction. Indeed, the ground state for a small NC of negative K_1 is expected to be F<111> because the magnetocrystalline energy is minimized for M parallel to <111>. Surprisingly, for a large M_S =1.95 MA/m, the ground state in small NCs of negative K_1 is F<001>. The large saturation magnetization imposes here a F<001> hard-axis flower state because it allows reducing the dipolar energy thanks to the alignement of the moments mainly parallel to the faces. In this case, the easy-axis flower F<111> is never observed, the transition only involves hard-axis flower and vortex, *i.e.* F<001> and V<001>.

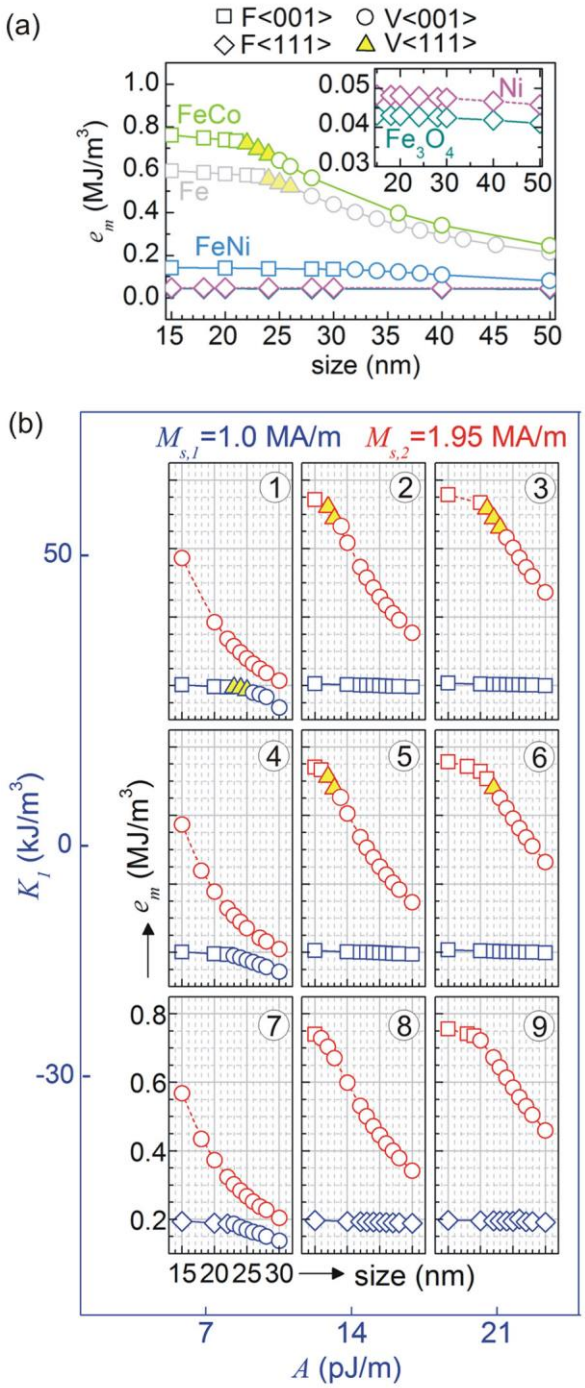

Figure 5. (a) Size dependence of the total magnetic energy density for NCs composed of the magnetic materials listed in the Table 1. (b) Size dependence of the total magnetic energy density for M_S = 1.0 MA/m (blue) and 1.95 MA/m (red). Cubic magnetocrystalline constant decreases from the top to the bottom: K_1 = 50 kJ/m^3 (frames 1,2,3), 0 kJ/m^3 (frames 4,5,6), and -30 kJ/m^3 (frames 7,8,9). Exchange constant increases from left to right: A = 7 pJ/m (frames 1,4,7), 14 pJ/m (frames 2,5,8) and 21 pJ/m (3,6,9).

While K_1 does not significantly modify the critical size, which is found at ~20 nm for M_S = 1.95 MA/m and A = 21 pJ/m whatever the considered K_1 value, it does influence the stability of V<111>. A major point is that negative K_1 values do not induce V<111>, contrarily to positive K_1, even though it would correspond to an easy-axis vortex. This difference is attributed to a reduced K_{mc} energy density in V<111> NCs of positive cubic MCA, as illustrated in the V<111> region of Fig. 1(a) and 4(d). Despite a weak magnetocrystalline energy value compared to exchange and dipolar energies, MCA plays a key role in the stability of intermediate V<111> states. Surprisingly, NCs exhibiting K_1 = 0 can present V<111> as ground states in the flower/vortex transition, contrarily to the previous predictions that V<111> was a metastable solution for zero anisotropy NC [14].

Consequently, V<111> can only be stabilized in materials which exhibit a fairly large M_S and a zero or positive cubic MCA K_1. Such features can be found in nearly cubic crystalline and amorphous Fe and FeCo nanocuboids.

7. Conclusion

Phase diagrams of rectangular nanocuboids made of cubic MCA materials have been investigated in the flower/vortex transition size range. We have demonstrated that a V<111> state appears as an intermediate state for NCs of zero and positive cubic MCA. It excludes Fe_3O_4 and Ni particles of negative cubic MCA. Simulations also indicate that deviations from the perfect cubic shape may suppress V<111> states (above 12% of deviation) and impact F<001> and V<001> configurations close to the transition critical size. The magnetization reversal of NCs presenting a V<111> as virgin state can be described as the progressive rotation of the whole vortex structure as a function of an applied field along one NC edge. The remanent state corresponds to a V<111> state allowing to experimentally observe V<111> state in previously saturated NCs made of adequate materials. The small magnetic

volume of NCs exhibiting V<111> configuration combined with the strict material and shape limitation makes the observation of V<111> spin configurations in real systems highly challenging.

Author information

Corresponding Author

*Blon Thomas, thomas.blon@insa-toulouse.fr

Present adress:

† Francisco Bonilla, fbonilla@cicenergigune.com, +34 945 297 108, CIC energigune, Parque Tecnológico de Álava, Albert Einstein 48 - ED. CIC, 01510, Miñano, Spain.

Conflict of Interest: The authors declare no competing financial interest.

Acknowledgements

We thank Julian Carrey for his careful reading of the manuscript and fruitful discussions. This work was supported by the French national project EMMA (ANR12 BS10 013 01).

References

[1] B. Mehdaoui , A. Meffre , J. Carrey, S. Lachaize , L-M. Lacroix, M. Gougeon , B. Chaudret, M. Respaud, *Adv. Funct. Mater.* **21**, 4573–4581 (2011)

[2] L.-M. Lacroix, S. Lachaize, A. Falqui, T. Blon, J. Carrey, M. Respaud, F. Dumestre, C. Amiens, O. Margeat, B. Chaudret, P. Lecante, and E. Snoeck, *J. Appl. Phys.* **103**, 07D521 (2008).

[3] L. Lartigue, D. Alloyeau, J. Kolosnjaj-Tabi, Y. Javed, P. Guardia, A. Riedinger, C. Péchoux, T. Pellegrino, C. Wilhelm, and F. Gazeau, *ACS Nano* **7**, 3939 (2013).

[4] S. Mitra, S. Das, K. Mandal and S. Chaudhuri, *Nanotechnology* **18**, 275608 (2007).

[5] Qing Song and Z. John Zhang, *J. Am. Chem. Soc.* **126**, 6164 (2004).

[6] M. Wang, L. Zeng and Q. Chen, *Dalton Trans.* **40**, 597 (2011).

[7] D. Kodama, K. Shinoda, K. Sato, Y. Konno, R.J. Joseyphus, K. Motomiya, H. Takahashi, T. Matsumoto, Y. Sato, K. Tohji, and B. Jeyadevan, *Adv. Mater.* **18**, 3154 (2006).

[8] M. Chen, J. Kim, J.P. Liu, H. Fan, and S. Sun, J. Am. Chem. Soc. **128**, 7132 (2006)

[9] A.P. LaGrow, B. Ingham, S. Cheong, G.V.M. Williams, C. Dotzler, M.F. Toney, D.A. Jefferson, E.C. Corbos, P.T. Bishop, J. Cookson, and R.D. Tilley, *J. Am. Chem. Soc.* **134**, 855 (2012).

[10] W.F. Brown, *Ann. N. Y. Acad. Sci*. **147**, 463 (1969).

[11] M.E. Schabes and H.N. Bertram, *J. Appl. Phys.* **64**, 1347 (1988).

[12] http://www.ctcms.nist.gov/~rdm/mumag.org.html

[13] N.A. Usov and S.E. Peschany, *J. Magn. Magn. Mater.* **110**, L1 (1992).

[14] W. Rave, K. Fabian, and A. Hubert, *J. Magn. Magn. Mater.* **190**, 332 (1998).

[15] R. Hertel and H. Kronmüller, *J. Magn. Magn. Mater.* **238**, 185 (2002).

[16] P. Vargas, D. Altbir, J. d'Albuquerque e Castro, *Phys. Rev. B* **73**, 092417 (2006).

[17] K. Fabian, A. Kirchner, W. Williams, F. Heider, T. Leibl, and A. Huber, *Geophys. J. Int.* **124**, 89 (1996).

[18] L. Hua, J.E.L. Bishop, and J.W. Tucker, *IEEE Trans. Magn.* **30**, 760 (1994).

[19] C. Gatel, F.J. Bonilla, A. Meffre, E. Snoeck, B. Warot-Fonrose, B. Chaudret, L.-M. Lacroix, and T. Blon, *Nano Lett.* **15**, 6952 (2015).

[20] D. Reyes, N. Biziere, B. Warot-Fonrose, T. Wade, and C. Gatel, *Nano Lett.* **16**, 1230 (2016).

[21] J.M. Thomas, E.T. Simpson, T. Kasama, and R.E. Dunin-Borkowski, *Acc. Chem. Res.* **41**, 665 (2008).

[22] T.P. Almeida, T. Kasama, A.R. Muxworthy, W. Williams, L. Nagy, R.E. Dunin-Borkowski, *Geophys. Res. Lett.* **41** 7041-7047 (2014).

[23] A. Kákay and L.K. Varga, *J. Appl. Phys.* **97**, 083901 (2005).

[24] Donahue, M.J.; Porter, D.G. OOMMF User's Guide, Version 1.0, Interagency Report NISTIR 6376, National Institute of Standards and Technology, Gaithersburg, MD (1999)

[25] A.R. Muxworthy and W. Williams, *Geophys. J. Int.* **202**, 578 (2015).

[26] J.M.D. Coey, *Magnetism and Magnetic Materials* (Cambridge University Press, Cambridge, 2010).

[27] H.F. Schmidts and H. Kronmüller, *J. Magn. Magn. Mater.* **94**, 220 (1991).

[28] W. Rave, K. Ramstöck, and A. Hubert, *J. Magn. Magn. Mater.* **183**, 329 (1998).

[29] Y. Nakatani, Y. Uesaka, and N. Hayashi, *Jpn. J. Appl. Phys.* **28**, 2485 (1989).

[30] C.E. Johnson and W.F. Brown, *J. Appl. Phys.* **32**, S243 (1961).

[31] N.A. Usov and S.E. Peschany, *J. Magn. Magn. Mater.* **174**, 247 (1997).

[32] S. Vock, C. Hengst, M. Wolf, K. Tschulik, M. Uhlemann, Z. Sasvári, D. Makarov, O.G. Schmidt, L. Schultz, and V. Neu, *Appl. Phys. Lett.* **105**, 172409 (2014).

[33] D. Betto and J.M.D. Coey, *J. Appl. Phys.* **115**, 17D138 (2014).

[34] A. Witt, K. Fabian, U. Bleil, *Earth Planet. Sci. Lett.* **233**, 311-324 (2005)

[35] E. Snoeck, C. Gatel, L.M. Lacroix, T. Blon, S. Lachaize, J. Carrey, M. Respaud, and B. Chaudret, *Nano Lett.* **8**, 4293 (2008).